JOURNAL OF THE AMERICAN CHEMICAL SOCIETY

Subscriber access provided by UNIV TORONTO

Article

Revealing High Na-Content P2-Type Layered Oxides for Advanced Sodium-Ion Cathodes

Chenglong Zhao, Zhenpeng Yao, Qidi Wang, Haifeng Li, Jianlin Wang, Ming Liu, Swapna Ganapathy, Yaxiang Lu, Jordi Cabana, Baohua Li, Xuedong Bai, Alán Aspuru-Guzik, Marnix Wagemaker, Liquan Chen, and Yong-Sheng Hu

J. Am. Chem. Soc., **Just Accepted Manuscript** • DOI: 10.1021/jacs.9b13572 • Publication Date (Web): 02 Mar 2020

Downloaded from pubs.acs.org on March 2, 2020

Just Accepted

“Just Accepted” manuscripts have been peer-reviewed and accepted for publication. They are posted online prior to technical editing, formatting for publication and author proofing. The American Chemical Society provides “Just Accepted” as a service to the research community to expedite the dissemination of scientific material as soon as possible after acceptance. “Just Accepted” manuscripts appear in full in PDF format accompanied by an HTML abstract. “Just Accepted” manuscripts have been fully peer reviewed, but should not be considered the official version of record. They are citable by the Digital Object Identifier (DOI®). “Just Accepted” is an optional service offered to authors. Therefore, the “Just Accepted” Web site may not include all articles that will be published in the journal. After a manuscript is technically edited and formatted, it will be removed from the “Just Accepted” Web site and published as an ASAP article. Note that technical editing may introduce minor changes to the manuscript text and/or graphics which could affect content, and all legal disclaimers and ethical guidelines that apply to the journal pertain. ACS cannot be held responsible for errors or consequences arising from the use of information contained in these “Just Accepted” manuscripts.

is published by the American Chemical Society. 1155 Sixteenth Street N.W., Washington, DC 20036

Published by American Chemical Society. Copyright © American Chemical Society. However, no copyright claim is made to original U.S. Government works, or works produced by employees of any Commonwealth realm Crown government in the course of their duties.

Revealing High Na-Content P2-Type Layered Oxide as Advanced Sodium-Ion Cathodes

Chenglong Zhao,[1,2†] Zhenpeng Yao,[3†] Qidi Wang,[4,5†] Haifeng Li,[6] Jianlin Wang,[7] Ming Liu[8], Swapna Ganapathy[8], Yaxiang Lu,[1,2] Jordi Cabana,[6] Baohua Li,[4] Xuedong Bai,[7] Alán Aspuru-Guzik,[3,9] Marnix Wagemaker,[8]* Liquan Chen[1], and Yong-Sheng Hu[1,2,10]*

[1]Key Laboratory for Renewable Energy, Beijing Key Laboratory for New Energy Materials and Devices, Beijing National Laboratory for Condensed Matter Physics, Institute of Physics, Chinese Academy of Sciences, Beijing 100190, China.
[2]Center of Materials Science and Optoelectronics Engineering, University of Chinese Academy of Sciences, Beijing 100049, China.
[3]Department of Chemistry and Chemical Biology, Harvard University, Cambridge, MA, 02138, USA.
[4]Division of Energy and Environment, Engineering Laboratory for the Next Generation Power and Energy Storage Batteries Graduate School at Shenzhen, Tsinghua University, Shenzhen 518055, China.
[5]School of Materials Science and Engineering Tsinghua University, Beijing 100084, China.
[6]Department of Chemistry, University of Illinois at Chicago, Chicago, Illinois 60607, United States.
[7]State Key Laboratory for Surface Physics, Institute of Physics, Chinese Academy of Sciences, Beijing, 100190, China.
[8]Department of Radiation Science and Technology, Delft University of Technology, Mekelweg 15, 2629JB Delft, the Netherlands.
[9]Department of Chemistry and Department of Computer Science, University of Toronto, Toronto, Ontario M5S 3H6, Canada.
[10]Yangtze River Delta Physics Research Center Co. Ltd, Liyang 213300, China.

KEYWORDS. P2-type oxide, High Na content, Cathode, multi-electron reaction, Na-ion battery

ABSTRACT: Layered Na-based oxides with the general composition Na_xTMO_2 (TM=transition metal) have attracted significant attention for their high compositional diversity that provides tuneable electrochemical performance for positive electrodes in in sodium-ion batteries. The various compositions bring forward complex structural chemistry that is decisive for the layered stacking structure, Na-ion conductivity and the redox-activity, potentially promising new avenues in functional material properties. In this work, we have explored the maximum Na content in these P2-type layered oxides, and discovered that the high-content Na in host enhances the structural stability, moreover, it promotes the oxidation of low-valent cations to their high oxidation states (in this case Ni^{2+}). This can be rationalized by the increased hybridization of the O(2p)-TM(3d-e_g) states, affecting both the local TM environment as well as the interactions between the NaO_2 and TMO_2 layers. These properties are highly beneficial for the Na storage capabilities as required for positive electrodes in sodium-ion batteries. It leads to excellent Na-ion mobility, a large storage capacity (>100 mAh g^{-1}), yet preventing the detrimental sliding of the TMO_2 layers (P2-O2 structural transition), as reflected by the ultra-long cycle life (3000 (dis)charge cycles demonstrated). These findings expand the horizons of high Na-content P2-type materials, providing new insights of the electronic and structural chemistry for advanced cathode materials.

1 Introduction

Sodium-ion batteries (NIBs) have been gaining much attention in battery field, both academic and industrial, owing to their potential application in large-scale electrical energy storage systems (EESs).[1-3] Significant efforts have been made in finding suitable electrode materials with desired properties, and the determination of structure-property relationships. Because of the large compositional diversity of the structural chemistry, layered oxides are considered as one of the most important electrodes families for NIBs, where the electrochemical performance can be tailored via the introduction of different elements in the hosts.

Na-based layered oxides with the general formula of Na_xTMO_2 (TM: transition metal) can be categorized into two main structures, O3- and P2-type phases, unlike the layered electrodes of Li-ion batteries (LIBs), which mostly crystallize in the O3-type structure. O represents that Na ions are accommodated at the octahedral (O) sites and P denotes Na ions at trigonal prismatic (P) sites; the number 2 or 3 represents the number of edge-sharing TMO_6 octahedra with the oxygen stacking in ABBA or ABCABC packing (Figure S1), respectively.[4] It is noteworthy that these layered oxides often experience detrimental phase transitions between O- and P-type structures during the charge-discharge process, making it a challenge to realize good cycling performance. Compared to the O3-type framework, the P2 structure enable the fast Na^+ diffusion owing to the open prismatic diffusion pathways between the TMO_2 slabs shown in Figure S1.[5-6] This provides the opportunity to achieve high cycle/rate capabilities.

However, it is established that P2-type electrodes usually deliver a low initial charge capacity of ~80 mAh g^{-1} below 4.0 V [7-15] or a low average voltage <3.2 V [11, 13, 16-17] (Figure S2a). Additionally, they suffer from the detrimental phase transition from P2 to O2 or OP4/'Z' phases upon charging (desodiation) in Figure 1a, which compromises the cycling stability.[7, 9, 12-13, 16, 18]

In order to enhance the properties of P2-type materials ion-substitution and/or doping, with Li^+, Mg^{2+}, Al^{3+}, Ti^{4+}, and Zn^{2+}, having no or fully occupied *d* orbitals[19-22] and Cu^{2+} inducing the Jahn-Teller effect[13], are widely used to alleviate the structural instability. For example, it has been demonstrated that using 5% mol Mg substituting Ni in $Na_{2/3}Ni_{1/3}Mn_{2/3}O_2$ can inhibit the global O2 phase transition to some extent, but instead a local OP4/'Z' phase transition is induced.[13] On the other hand, to obtain an increased charge capacity of >100 mAh g^{-1} below 4.0 V, the TM^{3+}-based P2-type oxides with TMs, such as Mn^{3+}[12], Fe^{3+}[9] and Co^{3+}[23], have been studied. However, the redox potential of these P2-type cathodes is generally lower than 3.0 V, compromising the overall energy density of the battery, and they often suffer from structural transitions in both the high-voltage (P2 to O2, OP4/'Z') and low-voltage (P2 to P'2) regions. An another disadvantage is that these materials are often sensitive to water and moisture in air.[24] From the above, it is clear that it is challenging to realize all demands simultaneously, for which more fundamental understanding is crucial.

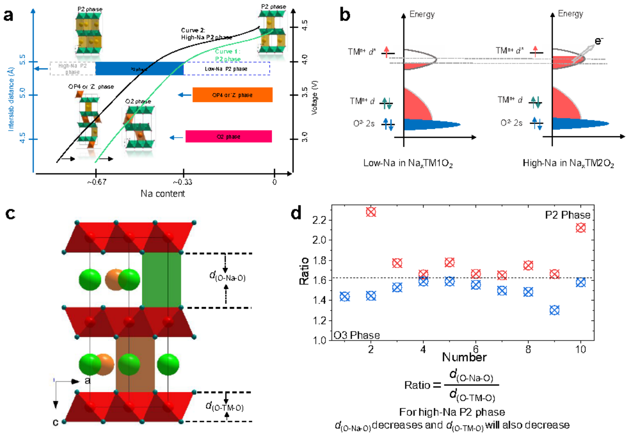

Figure 1. Possible advantages of the high-Na P2-type Na-ion cathodes and the corresponding design strategy. **a.** Structural evolution mechanism of high-Na P2 oxides during desodiation. **b.** The electronic structure of the low-Na and high-Na P2 oxides. **c.** Crystal structure of P2-type oxides. The interlayer distance $d_{(O\text{-}Na\text{-}O)}$ is the average perpendicular distance between the two oxygen sheets enclosing Na ions, and the interlayer distance $d_{(O\text{-}TM\text{-}O)}$ is the perpendicular distance of two parallel sheets containing transition metal (TM). **d.** The ratio between the interlayer distances of $d_{(O\text{-}Na\text{-}O)}$ and $d_{(O\text{-}TM\text{-}O)}$ for the typical P2- and O3-type compounds[25].

A key factor in the structural stability of the P2 host is the Na content. Na^+ shields the electrostatic repulsions between the TMO_2 slabs, in which during the desodiation in charge process, the decreased shielding of Na will drive the gliding of the TMO_2 slabs, resulting in the structural transition between the P- to O-type stackings. Therefore, if more Na can be retained in the P2 host upon charging (desodiation), the structural stability can be better maintained during the charge-discharge process. In addition, by analysing the electrochemical performance of P2 and O3 Na-ion cathodes (Figure S2a and b), we find that O3-type cathodes usually show a higher Na storage capacity than P2-type cathodes in a stable voltage window of 2.0-4.0 V, which is most likely related to the larger initial Na composition (x=1) of the hosts. A large amount of Na in P2-type materials can be expected to lower the average oxidation state of the TM ions than that of commonly low Na-content P2 materials, which can raise the 3*d* t_{2g} level of TMs. As a result, the larger number of electrons on the hybrid O(2*p*)-TM(3*d*-e_g) orbital will be more accessible at a relatively lower charge voltage, facilitating the charge-transfer reaction. Therefore, an important goal is to develop P2 materials with high Na content, so that more Na^+ to be retained in the NaO_2 slabs to prevent the structure transition, while reaching or exceeding the capacity of low Na-content P2 materials (x=2/3).

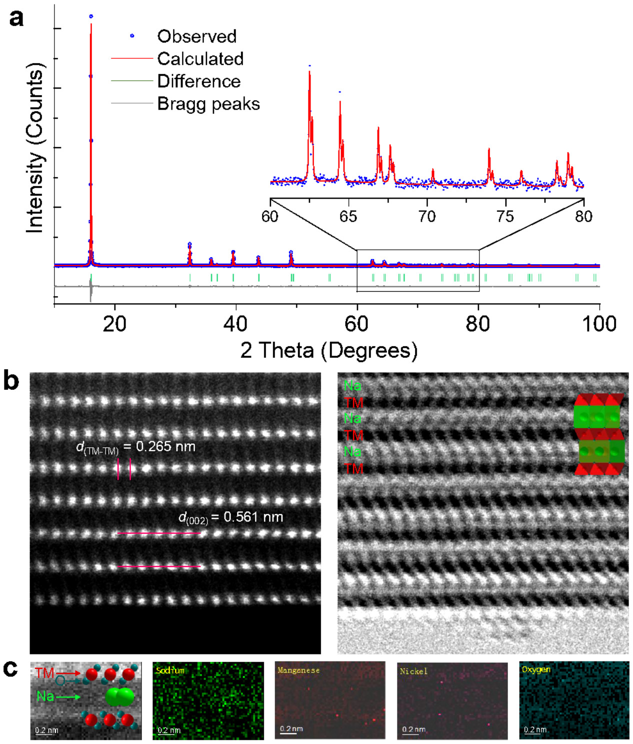

Figure 2. Structural characterization of the high Na-content P2 type oxide. **a**, Rietveld refinement of X-ray diffraction (XRD) pattern of $Na_{45/54}Li_{4/54}Ni_{16/54}Mn_{34/54}O_2$ (*a* = 2.89058(7) Å, *c* = 11.07541(18) Å), and the inset showing the enlarged pattern of (002) peak. **b**, Atomic-resolution high-angle annular dark field (HAADF) and annular bright field (ABF)-scanning transmission electron microscopy (STEM) images at the [010] zone axis. **c**, Electron energy loss spectroscopy (EELS) mappings of Na, Mn, Ni, and O elements.

To achieve high Na-content P2 materials we pursue the following rational design strategy. Based on our understanding of Na-ion intercalation chemistry[25], the ratio between the interlayer distances of $d_{(O\text{-}Na\text{-}O)}$ and $d_{(O\text{-}TM\text{-}O)}$ can be used as an indicator to distinguish structural competition between P2- and O3-type layered Na-ion oxides. The interlayer distance $d_{(O-Na-O)}$ is the average perpendicular distance between the two oxygen sheets enclosing Na ions, and the interlayer distance $d_{(O-TM-O)}$ is the perpendicular distance of two parallel sheets containing transition metal (TM). This interlayer distance is a result of the interactions of electrostatic cohesion forces and electrostatic repulsive forces between the NaO_2 layers and TMO_2 slabs. As for the high-Na P2-type oxides, the interlayer distance of $d_{(O-Na-O)}$ will decrease, because the increased Na content will raise the electrostatic cohesion forces between Na^+ and O^{2-} layers. If we assume that the interlayer distance $d_{(O-TM-O)}$ is the determining descriptor, a potential strategy is to substitute TMs in Na_xTMO_2 with cations having a smaller ion-size and higher oxidation state. Following this strategy we used P2-type $Na_{2/3}Ni_{1/3}Mn_{2/3}O_2$ as a starting model, which features a large fraction of Mn^{4+} in the host, having a small ion radius of $R_{CN=6} = 0.53$ Å[26]. It represents a typical low Na content (x=2/3) electrode, exhibiting a low initial charge capacity of ~80 mAh g^{-1} below 4.1 V accompanied by the detrimental P2 to O2 phase transition.[27] In this work, the Na content in P2 material was systematically varied from 2/3 to 1 mol per unit by introducing different elements into the pristine structure, such as Li^+, Mg^{2+}, Cu^{2+}, Mn^{3+}, Fe^{3+}, and Ti^{4+}, to substitute the Mn^{4+}/Ni^{2+}. Through this approach, several high Na-content materials were obtained with a Na content between 42/54 to 45/54 mol per unit.

2 Results

2.1 Structural analysis

In this work, $Na_{45/54}Li_{4/54}Ni_{16/54}Mn_{34/54}O_2$, was prepared based on the known P2-type $Na_{2/3}Ni_{1/3}Mn_{2/3}O_2$ through the same synthesis method (see Methods). In this as-prepared material, 34/54 mol Mn ions and 16/54 mol Ni ions exist in the tetravalent state and divalent state, as in the $Na_{2/3}Ni_{1/3}Mn_{2/3}O_2$ material. Ni^{2+} is used to serves as the redox centre due to the relatively high redox potential and promising two-electron transfer reaction of Ni^{2+}/Ni^{4+}. A large amount of Mn^{4+} is used as the structure former for its high abundance. The small fraction of Li^+ allows an increase in Na composition to balance the charge. Inductively coupled plasma atomic emission spectrometry (ICP-AES) analysis confirms the composition of $Na_{0.85}Li_{0.08}Ni_{0.30}Mn_{0.62}O_2$ (table S1). The morphology of this as-prepared material is characterized by scanning electron microscopy (SEM) (Figure S3), displaying plate-like particles with a distribution of sizes in the range of 8~12 μm. The crystal structure and phase purity were evaluated by Rietveld refinement analysis of the X-ray diffraction (XRD) pattern presented in Figure 2a. All the diffraction peaks can be indexed by the hexagonal structure with the space group of *P*6$_3$*/mmc,* reflecting the disordered Ni/Mn distribution. Crystallographic data, atomic coordinates, occupancies and anisotropic displacement parameters of this structure are listed in table S2 and S3. Compared to the lattice parameters of $Na_{2/3}Ni_{1/3}Mn_{2/3}O_2$[28] ($a$ = 2.885 Å, c = 11.155 Å), those of $Na_{0.85}Li_{0.08}Ni_{0.30}Mn_{0.62}O_2$ (a = 2.89058(7) Å and c = 11.07541(18) Å) indicate an expanded *a*-*b* plane and a contracted *c* axis, originating from an increased Na^+-Na^+ electrostatic repulsions in the NaO_2 in-plane direction and an increased O^{2-}-Na^+-O^{2-} electrostatic cohesions between NaO_6 and TMO_6 polyhedra, respectively. The ratio between the interlayer distances of $d_{(O-Na-O)}$ and $d_{(O-TM-O)}$ is calculated as 1.86, larger than the boundary of 1.62 which leads to a P2-type layered oxide. The detailed crystal structure is further investigated by high-resolution transmission electron microscopy (HRTEM), where the interplanar distance between the adjacent lattice fringes corresponds to the *d* spacing value of the (002) planes of the obtained P2 phase (Figure S4). Na ions occupy two kinds of trigonal prismatic sites, amounting 0.536 mol in the 2*d* site and 0.313 in the 2*b* site. The prismatic NaO_6 2*b* site shares two faces with the lower and upper octahedral TMO_6, which can be expected to be less stable than the that 2*d* site sharing edges with six octahedral TMO_6. The TM columns of Ni and Mn positions are revealed by spherical aberration-corrected scanning transmission electron microscopy (STEM) shown in Figure 2b, where both high angle annular dark-field (HAADF) and annular bright-field (ABF) images are provided for comparison. The faint bright contrast represents the Na and O columns between the octahedral TMO_2 slabs in the ABF-STEM image which is consistent with P2-type structure as demonstrated by the inset. The distance of the adjacent layer $d_{(TM-TM)}$ in HAADF-STEM image is measured to be ~0.558 nm, which corresponds to the interslab distance from the XRD refinement. Atomic-scale STEM image and electron energy loss spectroscopy (EELS) mappings of this P2-type material were carried out to confirm the elemental distribution, and the corresponding elemental mappings of Na, Mn, Ni and O are exhibited in Figure 2c. TM sites are occupied by Mn and Ni in a disordered arrangement, while Na locates in the sites between the TMO_2 layers.

2.2 Prediction of the stability of the high Na-content P2-type oxide

First-principles density functional theory (DFT)[29-31] calculations are used to explore the range of Na content in P2-type $Na_{12}LiNi_3Mn_8O_{24}$ oxide. We firstly study the Li/Mn/Ni ordering in the TM layer with a fully occupied Na layer (composition $NaLi_{1/12}Ni_{1/4}Mn_{2/3}O_2$). A P2-$NaTMO_2$ supercell with 12 metal sites was built, resulting in 910 symmetrically inequivalent configurations for the 1:3:8. Li:Ni:Mn ratio. The total energies of these configurations were evaluated and the one with the lowest energy is selected as the ground state of $Na_{12}LiNi_3Mn_8O_{24}$, as shown in Figure 3a. Using the as-identified $Na_{12}LiNi_3Mn_8O_{24}$ structure, we then explored symmetrically inequivalent Na/vacancy configurations at Na sites in $Na_{12}LiNi_3Mn_8O_{24}$ configuration for different compositions (Na/vacancy ratios). The $Na_{12-x}LiNi_3Mn_8O_{24}$ convex hull (Figure 3b) is constructed by calculating the formation energies of all configurations with respect to the end member phases. Two high Na-content phases are identified, having a Na composition of 9/12 and 10/12, which is larger than the well-known structure with a Na composition of 8/12 per super cell. The highest Na composition was further evaluated by a Na-Li-Ni-Mn-O phase diagram (in Figure S5), which demonstrates an energy of ~1.68 eV/atom lower than the combination of stable phases: $NaMnO_2$ + Li_2MnO_3 + $Na_2Mn_3O_7$ + Na_2O_2 + $NaNiO_2$. The predicted stability of the P2-type phase indicates the feasibility of preparing this material.

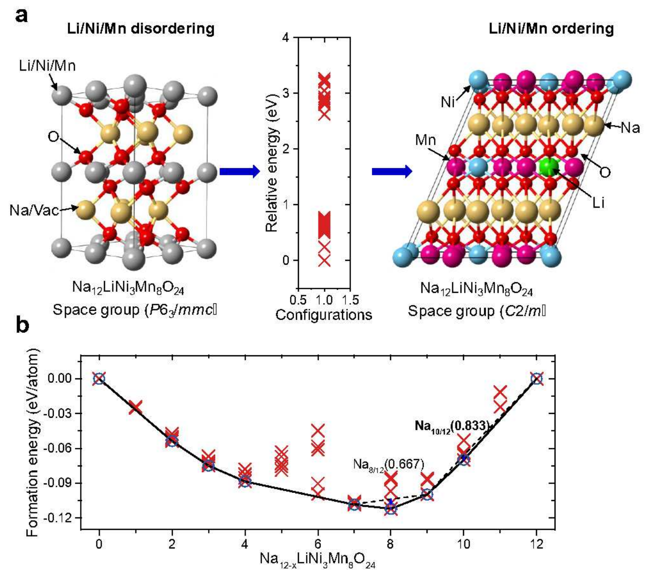

Figure 3. Determination the Na/vacancy ordering and phase stability in convex hull. a, Determination of the Li/Ni/Mn (dis)ordering in the system of $Na_{12-x}LiNi_3Mn_8O_{24}$. The detailed information of determination on the ground state structure and Li/Ni/Mn (dis)ordering in the system of $Na_{12-x}LiNi_3Mn_8O_{24}$ is presented in the Supporting discussion S1. **b**, Phase stability in $Na_{12-x}LiNi_3Mn_8O_{24}$-$LiNi_3Mn_8O_{24}$ convex hull. The formation energy was calculated considering all possible Na and their vacancy configurations, and the potential structures with different Na contents were predicted in this study. Red crosses indicate the energies of different enumerated phases computed at the Na content. Blue circles are ground states, as they are part of the convex energy hull in solid line.

2.3 Electrochemical performance

As shown in Figure 4a and b, this high Na-content P2-type cathode delivers a highly reversible capacity of ~102.5 mAh g^{-1} in the voltage range of 2.0-4.0 V, exceeding that of ~82 mAh g^{-1} for P2-type $Na_{2/3}Ni_{1/3}Mn_{2/3}O_2$. In $Na_{2/3}Ni_{1/3}Mn_{2/3}O_2$, the initial charge capacity has been demonstrated to originate from the single electron oxidation of the Ni^{2+}/Ni^{3+} redox couple below 4.0 V.[32] Interestingly, this high Na-content P2-type material contains a smaller amount of Ni^{2+} (16/54 mol) compared to 1/3 mol in $Na_{2/3}Ni_{1/3}Mn_{2/3}O_2$. Nevertheless, the as-prepared material exhibits a capacity that is 1.25 times higher in the same voltage range. The rate performance was also evaluated using electrodes with a relatively large mass loading of 8-10 mg cm^{-2} from 0.1C (16 mA g^{-1}) to 20C (3,200 mA g^{-1}) as shown in Figure 4c. When cycled at 10C, the capacity retention is ~ 65% of its initial capacity, corresponding to a current density of 1,600 mA g^{-1}. After the cycling rate test up to 20C, a reversible capacity of ~100 mAh g^{-1} is also reached at 0.5C, indicating excellent cyclability. The most appealing property of this as-prepared material is the ultra-long cycling stability as shown in Figure 4d, demonstrating more than 3,000 cycles with a good capacity retention of >68% at a current rate of 3.0C (540 mA g^{-1}). The average capacity decay is 0.012% per cycle. More than 70% of the capacity is retained up to 2,500 cycles with a CE that approaches 100%. Clearly, the present high Na-content material shows superior electrochemical properties compared to the reported low Na-content materials as shown in Figure S6 and S7.[7-15, 32]

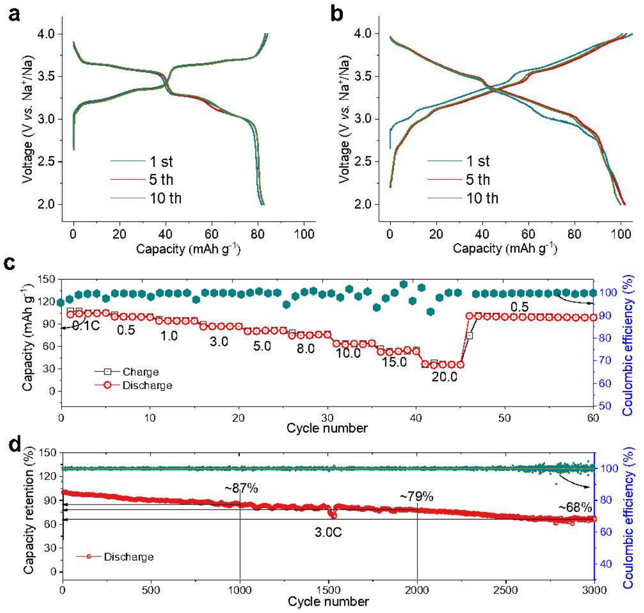

Figure 4. Electrochemical performance of high Na-content P2-type cathode. Galvanostatic charge-discharge curves of **a**, $Na_{2/3}Ni_{1/3}Mn_{2/3}O_2$ and **b**, $Na_{45/54}Li_{4/54}Ni_{16/54}Mn_{34/54}O_2$ electrodes at a rate of 0.15C (corresponding to ~22 mA g^{-1}) in the voltage range of 2.0-4.0 V *vs.* Na^+/Na. **c**, Rate capability of $Na_{45/54}Li_{4/54}Ni_{16/54}Mn_{34/54}O_2$ from 0.1C (16 mA g^{-1}) to 20C (3,200 mA g^{-1}). **c**, Discharge capacity retention of $Na_{45/54}Li_{4/54}Ni_{16/54}Mn_{34/54}O_2$ with first the three cycles at 0.1C (18 mA g^{-1}) and following cycled at 3.0C (540 mA g^{-1}). The capacity is normalized by that of 3.0C. Above 70 % capacity is retained up to 2,500 cycles with approximate 100% Coulombic efficiency (CE), but the CE is found to be unstable in the following cycles; after 3,000 cycles, ~68% capacity is remained.

2.4 Understanding the desodiation process and charge compensation

Although a cut-off voltage over 4.0 V will allow more Na^+ extraction from the host structure to provide a larger capacity, this usually results in structural degradation and electrolyte decomposition. When charged to 4.60 V, a capacity of ~150 mAh g^{-1} is obtained, corresponding to ~0.58 mol Na^+ being deintercalated in Figure 5a. However, it is worth noting that ~0.58 mol Na^+ is still lower than the maximum capacity from the two-electron transfer of 16/54 (~0.296) mol Ni^{2+} to Ni^{4+} per unit of $Na_{45/54}Li_{4/54}Ni_{16/54}Mn_{34/54}O_2$. To examine the origin of the charge compensation during the electrochemical desodiation, the formation energy during the charge process is evaluated as plotted in Figure 5b and 5c. Based on the calculated formation energies, the obtained voltage is in good agreement with the experimental observations. To obtain more insights into the redox activity, the magnetization of Ni and O ions are determined from DFT calculations, shown in Figure 5d and 4e, in which the number of unpaired electrons denote the oxidation states of the ions. Two intermediate phases are highlighted, x=5 and 7 in $Na_{10-x}LiNi_3Mn_8O_{24}$, where x=5 corresponds to the cut-off voltage at 4.0 V, and x=7 at 4.60 V. Further Nadeintercalation at higher potentials are not investigated due to the limited oxidation stability of the electrolyte. The calculated magnetization of Mn ions (Figure S8) indicates that Mn^{4+} does not participate in the redox reaction. It has recently been reported that Mn^{4+} can be oxidized to Mn^{7+} with the migration of Mn from octahedral sites to tetrahedral sites during the charge process[33], although no evidence of this was found in the current system.

Upon desodiation of $Na_{10-x}LiNi_3Mn_8O_{24}$ ($0 \leq x \leq 5$), Ni magnetization first decreases from 1.78 u_B (bohr magneton) to 1.077 u_B at x=3, corresponding to the oxidation from Ni^{2+} to Ni^{3+}. Meanwhile, the O magnetization maintains a value between 0.028 and 0.112 u_B, which indicates a relative constant redox state of the O^{2-} anion. This is also reflected by the partial density of states (pDOS) of the O 2*p* and Ni 3*d* orbitals shown in Figure 5f, in which Ni 3*d* t_{2g} orbitals have a much larger contribution to the valence band below the Fermi level (E_F) than the Mn 3*d* and O 2*p* states. Further desodiation to $Na_5LiNi_3Mn_8O_{24}$ (x=5), the decreased Ni magnetization indicates that all Ni^{2+} ions are oxidized to Ni^{3+} and 1/6 Ni^{3+} is further oxidized to Ni^{4+}. Meanwhile, the O ions remains in the O^{2-} state where O magnetization retains a value between 0.002 and 0.158 u_B. Based on the above results, the desodiation results in partial oxidation of Ni^{2+} to Ni^{4+} below charging to 4.0 V.

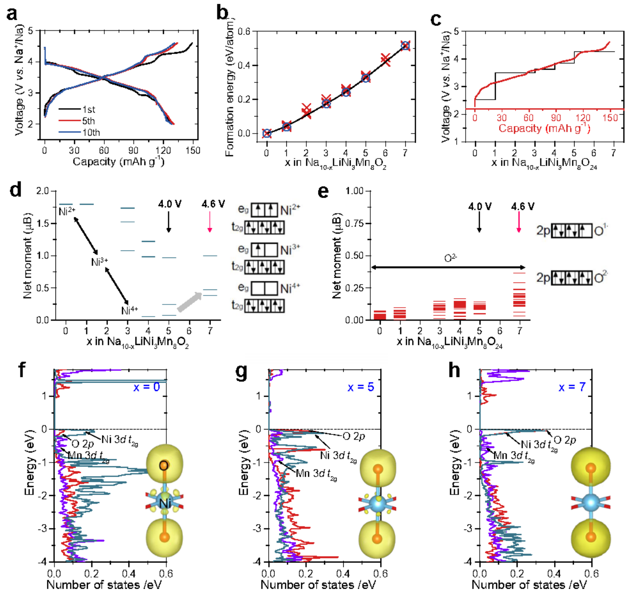

Figure 5. The desodiation process and redox sequence during the first charging process. a, Galvanostatic charge-discharge curves of $Na_{45/54}Li_{4/54}Ni_{16/54}Mn_{34/54}Li_{4/54}O_2$ at a rate of 0.15C in the voltage range of 2.0-4.60 V. **b** and **c**, The calculated formation energy of desodiation structures of $Na_{10-x}LiNi_3Mn_8O_{24}$ ($0 \leqslant x \leqslant 7$) convex hull and the corresponding voltage profile during the desodiation process in $Na_{45/54}Li_{4/54}Ni_{16/54}Mn_{34/54}O_2$. **d** and **e**, The magnetization and oxidation state evolution during the desodiation process of Ni and O ions in intermediate phases from $Na_{10}LiNi_3Mn_8O_{24}$ to $Na_3LiNi_3Mn_8O_{24}$. Electronic structure evolution on partial density of states (pDOS) of the Ni 3*d* t_{2g}, Mn 3*d* t_{2g} and O 2*p* orbitals of the x=0 (**f**), 5 (**g**), and 7 (**h**) in $Na_{10-x}LiNi_3Mn_8O_{24}$. The Fermi energy is set to 0 eV. Insets show the iso-surface of the charge density for the lowest unoccupied states of different desodiated states.

Upon further desodiation from $Na_5LiNi_3Mn_8O_{24}$ (x=5) to $Na_3LiNi_3Mn_8O_{24}$ (x=7), about 1/12 of O ions display an increase in the magnetic moment to 0.35 u_B. However, the Ni magnetization shows the opposite trend, indicating that Ni^{4+} is reduced while O^{2-} is oxidized. This suggests that there is a small amount of electron transfer from O^{2-} to Ni^{4+} at higher voltages (>4.2 V).[34-35] This internal interaction between O^{2-} to Ni^{4+} limits additional charge compensation and thus a higher capacity. Comparing the contributions of the O 2*p* and Ni 3*d* t_{2g} orbitals, it is observed that the latter still dominates the valence band immediately below the E_F level as shown in Figure 5g. This implies preferential electron extraction from Ni during charge ($Na_{10-x}LiNi_3Mn_8O_{24}$, $5 \leq x \leq 7$). On the other hand, during further desodiation, the Ni 3*d* states and O 2*p* states increasingly overlap near the E_F level in the valence band, as shown in Figure 5h.

Soft X-ray absorption spectroscopy (XAS), which can probe the bulk material up to a depth of 1~100 nm [36], has been widely used to investigate charge compensation mechanisms in electrode materials. Ni *L*-edge spectra of partial fluorescence yield (PFY) mode measurements were carried out at different states of charge (SOCs) shown in Figure S9. The split high-energy (L_3high) and low-energy (L_3low) features of the pristine spectrum demonstrate that Ni ions are in the divalent state, consistent with previous reports.[37] During the desodiation process, both Ni L_3- and L_2-edge sXAS spectra shift towards higher energies, which indicates that the Ni oxidation states increases. When increasing the potential from 3.5 V to 4.0 V the L_3high and L_2high features increase further, which indicates a mixture of Ni^{3+} and Ni^{4+} states.[37-38] Furthermore, at the SOC corresponding to 4.60 V, a delocalized hole density is found near the O orbitals surrounding Ni^{3+} and Ni^{4+}, which suggests the existence of the itinerant bands with a mixed O/Ni orbital symmetry. This agrees with the decreased Ni magnetization upon desodiation from $Na_5LiNi_3Mn_8O_{24}$ (x=5) to $Na_3LiNi_3Mn_8O_{24}$ (x=7) in Figure 5d. The features of pre-edge peak in the ligand O *K*-edge spectra can expose important information on the chemical bonding between ligand and TM atomic species. Generally, the pre-edge peaks in the range of 527 to 535 eV are due to the electronic transitions from the O 1*s* state to the O(2*p*)-TM(3*d*) hybridized states, which can be further divided into a lower energy peak of the band, and a higher peak of the O(2*p*)-TM(3*d*-e_g) hybridized states. The increase of O(2*p*)-TM(3*d*-e_g) hybridized state (in Figure S10 (a)) shows that oxidization of Ni creates more holes in the antibonding e_g orbital leading to the increase of the O *K*-edge in PFY mode measurements. This is further supported by the increasing overlap of Ni 3*d* states and O 2*p* states near the E_F level during desodiation, as shown in Figure 5h. The small amount of valence electrons in the desodiated sample promotes charge transfer from O to Ni via ligand-to-metal charge transfer in the local bonding configuration.[39] Furthermore, O *K*-edge spectra from surface-sensitive total electron yield measurements (TEY) demonstrate the presence of oxygen-containing decomposition products of the electrolyte and surface densification at 4.60 V. This can suppress the O(2*p*)-TM(3*d*) hybridization features for the electrodes resulting in a relative lower average valence state of Ni/Mn ions as shown in Figure S10 (b) and S11. [40] Meanwhile, the Mn *L*-edge PFY results show negligible changes upon cycling, as demonstrated in Figure S12, suggesting that the Mn^{4+} ions do not participate in the charge compensation[41], which is further confirmed by X-ray absorption near edge spectroscopy (XANES) spectra of the Mn *K*-edge at different states of charge as shown in Figure S13.

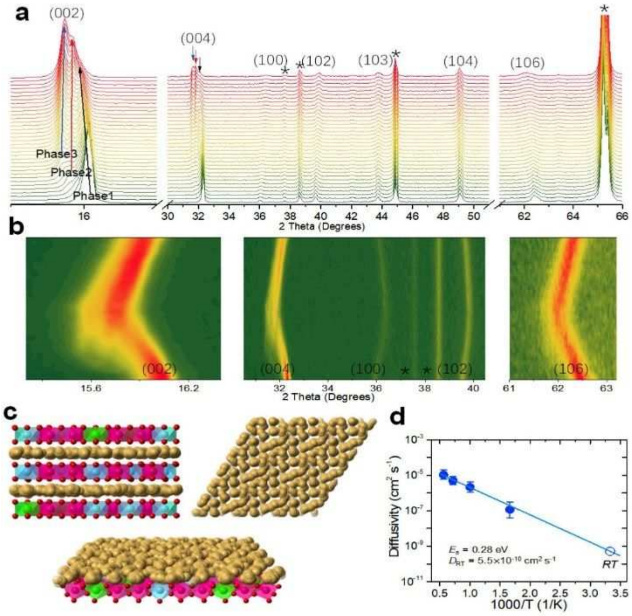

Figure 6. Structural evolution and Na^+ ion transport properties of this P2-type cathode. a, *In-situ* XRD patterns recorded at a rate of 0.05C charged to 4.60 V. The peaks marked by an asterisk originate from the casing of the *in-situ* Swagelok cell. **b,** *In-situ* XRD patterns recorded at a high rate of 0.5C in the voltage range 2.0-4.0 V. **c**, Na^+ migration pathway in the high Na-content P2-type oxide simulated at a temperature of ~1400 K over a period of 6 ps. The detailed views of Na^+ layers are given in the right and below panels, where the yellow spheres indicate the trace of the Na^+ positions during MD simulations. **d**, Arrhenius plot of diffusion coefficients resulting from the MD simulations, resulting in a Na^+ ion migration energy barrier of 0.28 eV.

2.5 Structural evolution

To explore the structural evolution of the high Na content cathode, *in-situ* XRD experiments are carried out during the charge-discharge process as shown in Figure 6a. From the onset of desodiation up to ~5 mAh g^{-1}, the (002) and (004) diffraction reflections slightly shift to a lower angle, while (100), (102), and (103) reflections move towards a higher angle. Subsequently, the (002) and (004) reflections become asymmetric and broader, and two new P2 phases (phase 2 and 3) appear upon further charging. The (002) reflection of the pristine P2 phase (phase 1) continuously shifts to lower angles, while the (002) reflections of the new P2 phases grow gradually without shifting, even up to the end of charge at 4.60 V. The main difference between these P2 phases is the Na content of the unit cell. [42 43 42 42 42 41 40 41 40 40 40 39 38] The material charged to 4.60 V can be fitted with three P2-Na_x $Li_{4/54}Ni_{16/54}Mn_{34/54}O_2$ phases having very similar cell parameters (as presented in Figure S14 and table S4). These three P2 phases can all be indexed by the hexagonal $P6_3/mmc$ symmetry with phase fractions of 5.1(2)%, 32.3(2)%, 62.6(2)%, and lattice parameters of a = 2.878(33) Å and c = 11.21(13) Å, a = 2.8668(4) Å and c = 11.2335(15) Å, a = 2.8135(13) Å and c = 11.2763(14) Å, respectively. The average Na content obtained from the refinement is ~0.24 mol, in good agreement with ICP results (~0.245 mol based on the normalized value of Mn). During the refinement, a relatively large 2*b* Na^+ occupation is found in the Na-poor phases. This indicates that Na^+ at the 2*d* sites is preferentially deintercalated from the structure, which should be expected based on the larger energy associated with occupying this site.[43-44] Another difference is the ~3.5 % difference in volume between the Na-poor P2 phase (phase 3) and pristine phase (phase 1). In addition, the Na-poor phase 2 and 3 exhibit a larger interlayer distance compared to phase 1. During desodiation, new P2 phases with a large interlayer distance are formed and their phase fractions increase simultaneously. At the same time, Na is mainly deintercalated from the pristine Na-rich P2 phase. The formation of the new P2 phases can be held responsible for the stability of the materials, as opposed to the commonly reported O2, OP4/'Z' phase transition upon desodiation.

During Na^+ intercalation upon discharging, the coexisting Na-poor and Na-rich phases gradually recombine to a single P2 phase as shown in Figure 6b. By fitting the XRD patterns at different charge-discharge states the (002) reflection becomes increasingly asymmetric due to a broad feature when fully discharging to 2.0 V, see Figure S15. To further study the structural stability after cycling, Rietveld refinement was conducted of an electrode after 100 cycles (*ex-situ*) as shown in Figure S16. All diffraction lines can be indexed with the hexagonal space group $P6_3/mmc$ and no additional diffraction peaks are detected. The lattice parameters are presented table S5 and S6. In contrast to the pristine P2-$Na_{45/54}Li_{4/54}Ni_{16/54}Mn_{34/54}O_2$ material, the lattice parameter evolution is highly reversible, reflecting the excellent cycling stability. The evolution of the structure is also studied at different current rates, the results of which are presented in Figure S17 and discussed in the Supplementary discussion S2.

Given the large Na^+ mobility for the P2-type structure, excellent electrode performance can be expected for the present high Na-content P2-type material. The Na^+ kinetics is studied by first-principle molecular dynamics (FPMD) simulations. Figure 6c exhibits the results of the FPMD simulations. The diffusion coefficients are determined from the Na^+ mean square displacements (MSDs) from simulations ranging from 600 to 1800 K (Figure S17). In Figure 6c, the Na^+ trajectories are displayed to illustrate the migration pathways. As expected, Na^+ migrates through the two-dimensional planes of the NaO_2 layers. As compared to the low Na-content material (0.667 mol), for the present high Na-content material the trajectories are more interconnected, showing much more jumps within the same simulation time.[5, 32] Figure 6d shows the Arrhenius plot of the calculated diffusion coefficient, resulting in a very low activation energy for diffusion (~0.28 eV) and a very large room temperature diffusion coefficient ($\sim 0.55\times10^{-10}$ cm^2 s^{-}

^{1}) as compared to layered Na cathodes[5-6, 12, 32, 42, 45], signifying the excellent Na^+ mobility of the present high Na content in P2-type material.

2.6 Accelerated aging measurement and full cells

To further study the chemical stability, the P2-type material was stored in air for half a year, after which it was soaked in deionized water for 2 h. The XRD patterns and the electrochemical results, shown in Figure S19 and S20, indicate that the material is stable against water and air. NIBs utilizing a hard carbon anode were assembled to investigate the full cell long-term cyclability of the high Na-content P2-type cathode, having a relatively high active mass loading of approximately 8 mg cm^{-2}, as shown in Figure S21-23. The electrochemical results show that the reversible capacity between 1.5 and 4.0 V is above 100 mAh g^{-1}, based on the mass of the cathode at a current rate of 0.1C at a high average operation voltage of ~3.3 V. The full cells display excellent capacity retention, exceeding >90 % over 400 cycles at 2.5C current rate.

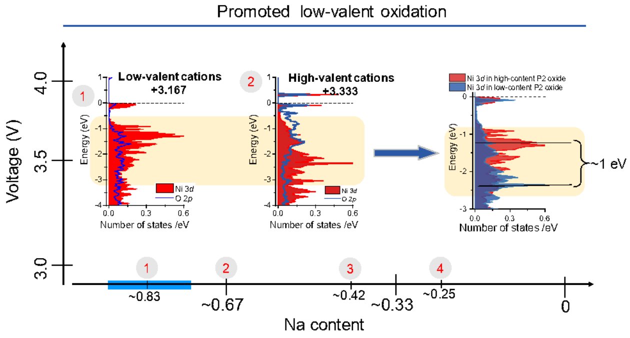

Figure 7. Illustration of the electronic evolution mechanism in the $Na_{45/54}Li_{4/54}Ni_{16/54}Mn_{34/54}O_2$ high Na-content P2-type material. The DFT predicted electronic evolution during charge (desodiation). The large amount of Na in P2-type materials reduces the average oxidation state of the TM ions below that of commonly low Na-content P2 materials. The consequence is that the low-valent cations can be oxidized to their high state more easily.

3 Discussion

The P2-type layered structure ensures facile Na^+ diffusion, however, the lower Na content (~2/3 mol per unit) usually compromises initial charge capacity and structural stability during the long-term cycling. The present exploration of high Na-content P2-type materials presents shows several advantageous properties.

(1) Promoting oxidization of the low-valent cations (*e.g.,* Ni^{2+}) to their high-valent states even at a relatively low cut-off charge voltage.

For the as-prepared high Na-content cathode, the Ni^{2+}/Ni^{4+} redox couple is successfully activated to provide additional capacity below 4.0 V, which is an essential ingredient for the design of high-performance Ni-based P2-type cathodes.[46] Generally, the redox reaction of Ni^{2+}/Ni^{4+} occurs at voltages around or exceeding 4.2 V. Such a higher redox potential introduces three issues, including structural transitions, electrolyte decomposition and activation of the oxygen redox causing oxygen loss, which will degrade the performance of the cathode material in terms of capacity and structural stability. Introducing a large amount of Na (0.75~0.83 mol per unit) into the P2-type material will make the average oxidation state of the TM ions lower than in low Na-content (~0.67 mol) P2 materials. In high Na-content P2 oxides, the lower average oxidation state of TMs can induce a larger contribution of low-valent cations in the valence band below the Fermi level, which provides additional capacity.

To rationalize this finding, DFT calculations were performed, the results of which are shown in Figure 7. Comparing the pDOS of P2-type $Na_{0.83}Li_{1/12}Ni_{1/4}Mn_{2/3}O_2$ and P2-type $Na_{0.67}Li_{1/12}Ni_{1/4}Mn_{2/3}O_2$ results in an average oxidation state of the TM ions of +3.167 and +3.333, respectively, where the former displays a larger contribution near the Fermi level. This implies easier participation of Ni^{2+} in the charge compensation upon desodiation. The disadvantage of the high Na-content P2 phase is that it is thermodynamically less stable compared to the low Na-content material, as demonstrated in Figure 3b. This is a result of the stronger Na^+-Na^+ electrostatic repulsions within the NaO_2 slabs (which may also contribute to the easier oxidation of Ni^{2+} to Ni^{4+} at low voltages). Recently, many disordered rock salt-type oxides have been explored as cathodes for Li-ion batteries, where, indeed, most of these materials are thermodynamically metastable, offering a higher capacity.[31, 47]

(2) Stabilizing P2-type structure to prevent degradation from structural instability

The large amount of Na in P2-type host structure can ensure a high structural stability in a large compositional range during the desodiation process, as demonstrated in Figure 7b. For low Na-content P2-type materials, structural transitions from P2 to O2 or OP4/'Z' occur for voltages below ~4.2 V when the Na content in structural host drops below 1/3 mol Na. The higher Na content allows to maintain more Na^+ in the interlayers when the same amount of Na is deintercalated. A smaller amount of Na in NaO_2 slabs will lower TM^{n+}-TM^{n+} and Na^+-TM^{n+} electrostatic repulsions, resulting in gliding of the TMO_2 slabs. This induces the undesired phase transitions with large volumetric changes and rapid capacity decay. Our results demonstrate that during desodiation of $Na_{45/54}Li_{4/54}Ni_{16/54}Mn_{34/54}O_2$, Na-poor phases have a similar structure as the pristine material. These newly formed phases have a larger interlayer distance compared to that of the pristine structure, which is expected to be beneficial for Na^+ migration. The phase fractions of these desodiated phases increases upon charging, and reversible transform back to the pristine structure upon discharging (sodiation).

4 Summary

In this work, we have explored the peculiar structural chemistry of a high Na-content P2-type. As a proof of concept, a high Na-content layered material, $Na_{45/54}Li_{4/54}Ni_{16/54}Mn_{34/54}O_2$, has been successfully prepared. It is revealed that the high Na-content promotes the oxidization of the low-valent cation (Ni^{2+}) to its high oxidation state at a low cut-off voltage upon desodiation (charge), and that this stabilizes the P2-type structure, which generally promotes Na-ion conductivity. For the application as electrode for NIBs, this results in several advantaged compared to known low Na-content P2 materials. $Na_{45/54}Li_{4/54}Ni_{16/54}Mn_{34/54}O_2$ is demonstrated to have a higher reversible capacity of >100 mAh g^{-1} accompanied by the favourable multi-electron reaction of the Ni^{2+}/Ni^{4+} redox couple within the stability window of typical electrolytes of 2.0 to 4.0 V. Additionally, stabilizing the P2-type structure leads to an ultra-long cycle life of up to 3,000 cycles in combination with good rate performance. The advantages of the presently developed high Na-content P2-type material motivate further exploration of high Na-content electrode materials for NIBs. Possible dopant/substituting elements that may enable alternative high Na-content P2-type materials are multi-valent elements (*e.g.*, Ca^{2+}, Mg^{2+}, Y^{3+}, La^{3+}), which, when located at the Na sites, will also promote the oxidation of TM ions and stabilize the structure upon (dis)charging. The present study also reveals a promising strategy to realize multi-electron transfer toward a high oxidation state, potentially relevant for other research, *e.g.,* catalysts[48].

ASSOCIATED CONTENT

Supporting Information. This material is available free of charge via the Internet at http://pubs.acs.org.

Detailed synthesis, characterization and calculation methods; Electrochemical cycling, SEM and TEM images; Stability evaluation; X-ray absorption spectra; XRD patterns; Structural parameters from Rietveld refinement.

AUTHOR INFORMATION

Corresponding Author

* m.wagemaker@tudelft.nl, yshu@aphy.iphy.ac.cn.

Author Contributions

‡These authors contributed equally.

Notes

The author declares no competing financial interest.

ACKNOWLEDGMENT

This work was supported by the National Key Technologies R&D Program of China (2016YFB0901500), the National Natural Science Foundation (NSFC) of China (51725206 and 51421002), NSFC-UKRI_EPSRC (51861165201), the Strategic Priority Research Program of the Chinese Academy of Sciences (XDA21070500), Beijing Municipal Science and Technology Commission (Z181100004718008), and Beijing Natural Science Fund-Haidian Original Innovation Joint Fund (L182056), the Center for Electrochemical Energy Science, an Energy Frontier Research Center funded by the U.S. Department of Energy (DOE), Office of Science, Basic Energy Science (#DE-FG02-17ER16362), the National Science Foundation under Grant No. DMR-1809372, and the Netherlands Organization for Scientific Research (NWO) under the VICI grant nr. 16122. C. Zhao also thanks to the State Scholarship Fund of China Scholarship Council (CSC).

REFERENCES

1. Dunn, B.; Kamath, H.; Tarascon, J.-M., Electrical Energy Storage for the Grid: A Battery of Choices. *Science* **2011,** *334* (6058), 928.
2. Hwang, J.-Y.; Myung, S.-T.; Sun, Y.-K., Sodium-ion batteries: present and future. *Chem. Soc. Rev.,* **2017,** *46* (12), 3529-3614.
3. Muñoz-Márquez, M. Á.; Saurel, D.; Gómez-Cámer, J. L.; Casas-Cabanas, M.; Castillo-Martínez, E.; Rojo, T., Na-Ion Batteries for Large Scale Applications: A Review on Anode Materials and Solid Electrolyte Interphase Formation. *Adv. Energy Mater.,* **2017,** *7* (20), 1700463.
4. Delmas, C.; Fouassier, C.; Hagenmuller, P., Structural classification and properties of the layered oxides. *Phys. B+C* **1980,** *99* (1), 81-85.
5. Wang, Y.; Xiao, R.; Hu, Y.-S.; Avdeev, M.; Chen, L., P2-$Na_{0.6}[Cr_{0.6}Ti_{0.4}]O_2$ cation-disordered electrode for high-rate symmetric rechargeable sodium-ion batteries. *Nat. Commun.,* **2015,** *6*, 6954.
6. Katcho, N. A.; Carrasco, J.; Saurel, D.; Gonzalo, E.; Han, M.; Aguesse, F.; Rojo, T., Origins of Bistability and Na Ion Mobility Difference in P2- and O3-$Na_{2/3}Fe_{2/3}Mn_{1/3}O_2$ Cathode Polymorphs. *Adv. Energy Mater.,* **2017,** *7* (1), 1601477.
7. Wang, P.-F.; You, Y.; Yin, Y.-X.; Wang, Y.-S.; Wan, L.-J.; Gu, L.; Guo, Y.-G., Suppressing the P2–O2 Phase Transition of $Na_{0.67}Mn_{0.67}Ni_{0.33}O_2$ by Magnesium Substitution for Improved Sodium-Ion Batteries. *Angew. Chem. Int. Ed.,* **2016,** *55* (26), 7445-7449.
8. Zhu, Y.-E.; Qi, X.; Chen, X.; Zhou, X.; Zhang, X.; Wei, J.; Hu, Y.; Zhou, Z., A P2-$Na_{0.67}Co_{0.5}Mn_{0.5}O_2$ cathode material with excellent rate capability and cycling stability for sodium ion batteries. *J. Mater. Chem. A* **2016,** *4* (28), 11103-11109.
9. Yabuuchi, N.; Kajiyama, M.; Iwatate, J.; Nishikawa, H.; Hitomi, S.; Okuyama, R.; Usui, R.; Yamada, Y.; Komaba, S., P2-type $Na_x[Fe_{1/2}Mn_{1/2}]O_2$ made from earth-abundant elements for rechargeable Na batteries. *Nat Mater* **2012,** *11* (6), 512-7.
10. de la Llave, E.; Nayak, P. K.; Levi, E.; Penki, T. R.; Bublil, S.; Hartmann, P.; Chesneau, F.-F.; Greenstein, M.; Nazar, L. F.; Aurbach, D., Electrochemical performance of $Na_{0.6}[Li_{0.2}Ni_{0.2}Mn_{0.6}]O_2$ cathodes with high-working average voltage for Na-ion batteries. *J. Mater. Chem. A* **2017,** *5* (12), 5858-5864.
11. Han, M. H.; Gonzalo, E.; Sharma, N.; López del Amo, J. M.; Armand, M.; Avdeev, M.; Saiz Garitaonandia, J. J.; Rojo, T., High-Performance P2-Phase $Na_{2/3}Mn_{0.8}Fe_{0.1}Ti_{0.1}O_2$ Cathode Material for Ambient-Temperature Sodium-Ion Batteries. *Chem. Mater.,* **2015,** *28* (1), 106-116.
12. Singh, G.; Tapia-Ruiz, N.; Lopez del Amo, J. M.; Maitra, U.; Somerville, J. W.; Armstrong, A. R.; Martinez de Ilarduya, J.; Rojo, T.; Bruce, P. G., High Voltage Mg-Doped $Na_{0.67}Ni_{0.3-x}Mg_xMn_{0.7}O_2$ (x = 0.05, 0.1) Na-Ion Cathodes with Enhanced Stability and Rate Capability. *Chem. Mater.,* **2016,** *28* (14), 5087-5094.
13. Zheng, L.; Li, J.; Obrovac, M. N., Crystal Structures and Electrochemical Performance of Air-Stable $Na_{2/3}Ni_{1/3-x}$CuxMn2/3O2 in Sodium Cells. *Chem. Mater.,* **2017,** *29* (4), 1623-1631.
14. Li, L.; Wang, H.; Han, W.; Guo, H.; Hoser, A.; Chai, Y.; Liu, X., Understanding Oxygen Redox in Cu-Doped P2-$Na_{0.67}Mn_{0.8}Fe_{0.1}Co_{0.1}O_2$ Cathode Materials for Na-Ion Batteries. *J. Electrochem. Soc.,* **2018,** *165* (16), A3854-A3861.
15. Lv, S.; Verhallen, T.; Vasileiadis, A.; Ooms, F.; Xu, Y.; Li, Z.; Li, Z.; Wagemaker, M., Operando monitoring the lithium spatial distribution of lithium metal anodes. *Nat. Commun.,* **2018,** *9* (1), 2152.
16. Mortemard de Boisse, B.; Carlier, D.; Guignard, M.; Bourgeois, L.; Delmas, C., P2-$Na_xMn_{1/2}Fe_{1/2}O_2$ phase used as positive electrode in Na batteries: structural changes induced by the electrochemical (de)intercalation process. *Inorg. Chem.,* **2014,** *53* (20), 11197-205.
17. Kang, S. M.; Park, J. H.; Jin, A.; Jung, Y. H.; Mun, J.; Sung, Y. E., Na^+/Vacancy Disordered P2-$Na_{0.67}Co_{1-x}Ti_xO_2$: High-Energy and High-Power Cathode Materials for Sodium Ion Batteries. *ACS Appl. Mater. Inter.,* **2018,** *10* (4), 3562-3570.
18. Talaie, E.; Duffort, V.; Smith, H. L.; Fultz, B.; Nazar, L. F., Structure of the high voltage phase of layered P2-$Na_{2/3-z}[Mn_{1/2}Fe_{1/2}]O_2$ and the positive effect of Ni substitution on its stability. *Energy Environ. Sci.,* **2015,** *8* (8), 2512-2523.
19. Zhang, X. H.; Pang, W. L.; Wan, F.; Guo, J. Z.; Lu, H. Y.; Li, J. Y.; Xing, Y. M.; Zhang, J. P.; Wu, X. L., P2-$Na_{2/3}Ni_{1/3}Mn_{5/9}Al_{1/9}O_2$ Microparticles as Superior Cathode Material for Sodium-Ion

Batteries: Enhanced Properties and Mechanisam via Graphene Connection. *ACS Appl. Mater. Inter.,* **2016,** *8* (32), 20650-9.

20. Wu, X.; Xu, G. L.; Zhong, G.; Gong, Z.; McDonald, M. J.; Zheng, S.; Fu, R.; Chen, Z.; Amine, K.; Yang, Y., Insights into the Effects of Zinc Doping on Structural Phase Transition of P2-Type Sodium Nickel Manganese Oxide Cathodes for High-Energy Sodium Ion Batteries. *ACS Appl. Mater. Inter.,* **2016,** *8* (34), 22227-37.

21. Kim, D.; Kang, S.-H.; Slater, M.; Rood, S.; Vaughey, J. T.; Karan, N.; Balasubramanian, M.; Johnson, C. S., Enabling Sodium Batteries Using Lithium-Substituted Sodium Layered Transition Metal Oxide Cathodes. *Adv. Energy Mater.,* **2011,** *1* (3), 333-336.

22. Xu, J.; Lee, D. H.; Clément, R. J.; Yu, X.; Leskes, M.; Pell, A. J.; Pintacuda, G.; Yang, X.-Q.; Grey, C. P.; Meng, Y. S., Identifying the Critical Role of Li Substitution in P2–$Na_x[Li_yNi_zMn_{1-y-z}]O_2$ (0 < x, y, z < 1) Intercalation Cathode Materials for High-Energy Na-Ion Batteries. *Chem. Mater.,* **2014,** *26* (2), 1260-1269.

23. Berthelot, R.; Carlier, D.; Delmas, C., Electrochemical investigation of the P2-Na_xCoO_2 phase diagram. *Nat. Mater.,* **2011,** *10* (1), 74-80.

24. Duffort, V.; Talaie, E.; Black, R.; Nazar, L. F., Uptake of CO2 in Layered P2-Na0.67Mn0.5Fe0.5O2: Insertion of Carbonate Anions. *Chem. Mater.,* **2015,** *27* (7), 2515-2524.

25. Zhao, C.; Avdeev, M.; Chen, L.; Hu, Y.-S., An O3-type Oxide with Low Sodium Content as the Phase-Transition-Free Anode for Sodium-Ion Batteries. *Angew. Chem. Int. Ed.,* **2018,** *57* (24), 7056-7060.

26. Shannon, R. D., Revised Effective Ionic Radii and Systematic Studies of Interatomic Distances in Halides and Chalcogenides. *Acta Crystallograp.,* **1976,** *A32*, 751-767.

27. Kubota, K.; Kumakura, S.; Yoda, Y.; Kuroki, K.; Komaba, S., Electrochemistry and Solid-State Chemistry of $NaMeO_2$ (Me = 3d Transition Metals). *Adv. Energy Mater.,* **2018,** *8* (17), 1703415.

28. Paulsen, J. M.; Donaberger, R. A.; Dahn, J. R., Layered T2-, O6-, O2-, and P2-Type $A_{2/3}[M'2+_{1/3}M^{4+}{}_{2/3}]O_2$ Bronzes, A = Li, Na; M' = Ni, Mg; M = Mn, Ti. *Chem. Mater.,* **2000,** *12* (8), 2257-2267.

29. Bai, Q.; Yang, L.; Chen, H.; Mo, Y., Computational Studies of Electrode Materials in Sodium-Ion Batteries. *Adv. Energy Mater.,* **2018,** *8* (17), 1702998.

30. Kang, K.; Meng, Y. S.; Bréger, J.; Grey, C. P.; Ceder, G., Electrodes with High Power and High Capacity for Rechargeable Lithium Batteries. *Science* **2006,** *311* (5763), 977.

31. Yao, Z.; Kim, S.; He, J.; Hegde, V. I.; Wolverton, C., Interplay of cation and anion redox in $Li_4Mn_2O_5$ cathode material and prediction of improved $Li_4(Mn,M)_2O_5$ electrodes for Li-ion batteries. *Sci. Adv.,* **2018,** *4* (5), eaao6754.

32. Wang, P.-F.; Yao, H.-R.; Liu, X.-Y.; Yin, Y.-X.; Zhang, J.-N.; Wen, Y.; Yu, X.; Gu, L.; Guo, Y.-G., Na^+/vacancy disordering promises high-rate Na-ion batteries. *Sci. Adv.,* **2018,** *4* (3), eaar6018.

33. Radin, M. D.; Vinckeviciute, J.; Seshadri, R.; Van der Ven, A., Manganese oxidation as the origin of the anomalous capacity of Mn-containing Li-excess cathode materials. *Nat. Energy* **2019,** *4* (8), 639-646.

34. Wang, X.; Liu, G.; Iwao, T.; Okubo, M.; Yamada, A., Role of Ligand-to-Metal Charge Transfer in O3-Type $NaFeO_2$–$NaNiO_2$ Solid Solution for Enhanced Electrochemical Properties. *J. Phys. Chem. C* **2014,** *118* (6), 2970-2976.

35. Asakura, D.; Okubo, M.; Mizuno, Y.; Kudo, T.; Zhou, H.; Amemiya, K.; de Groot, F. M. F.; Chen, J.-L.; Wang, W.-C.; Glans, P.-A.; Chang, C.; Guo, J.; Honma, I., Electron delocalization in cyanide-bridged coordination polymer electrodes for Li-ion batteries studied by soft x-ray absorption spectroscopy. *Phys. Rev. B* **2011,** *84* (4), 045117.

36. Lin, F.; Nordlund, D.; Markus, I. M.; Weng, T.-C.; Xin, H. L.; Doeff, M. M., Profiling the nanoscale gradient in stoichiometric layered cathode particles for lithium-ion batteries. *Energy Environ. Sci.,* **2014,** *7* (9), 3077-3085.

37. Qiao, R.; Wray, L. A.; Kim, J.-H.; Pieczonka, N. P. W.; Harris, S. J.; Yang, W., Direct Experimental Probe of the $Ni^{II}/Ni^{III}/Ni^{IV}$ Redox Evolution in $LiNi_{0.5}Mn_{1.5}O_4$ Electrodes. *J. Phys. Chem. C* **2015,** *119* (49), 27228-27233.

38. Piamonteze, C.; de Groot, F. M. F.; Tolentino, H. C. N.; Ramos, A. Y.; Massa, N. E.; Alonso, J. A.; Martínez-Lope, M. J., Spin-orbit-induced mixed-spin ground state in $RNiO_3$ perovskites probed by x-ray absorption spectroscopy: Insight into the metal-to-insulator transition. *Phys. Rev. B* **2005,** *71* (2), 020406.

39. Hong, J.; Gent, W. E.; Xiao, P.; Lim, K.; Seo, D.-H.; Wu, J.; Csernica, P. M.; Takacs, C. J.; Nordlund, D.; Sun, C.-J.; Stone, K. H.; Passarello, D.; Yang, W.; Prendergast, D.; Ceder, G.; Toney, M. F.; Chueh, W. C., Metal–oxygen decoordination stabilizes anion redox in Li-rich oxides. *Nat. Mater.,* **2019,** *18* (3), 256-265.

40. Qiao, R.; Liu, J.; Kourtakis, K.; Roelofs, M. G.; Peterson, D. L.; Duff, J. P.; Deibler, D. T.; Wray, L. A.; Yang, W., Transition-metal redox evolution in LiNi0.5Mn0.3Co0.2O2 electrodes at high potentials. *J. Power Sources* **2017,** *360*, 294-300.

41. Liang, X.; Pang, Q.; Kochetkov, I. R.; Sempere, M. S.; Huang, H.; Sun, X.; Nazar, L. F., A facile surface chemistry route to a stabilized lithium metal anode. *Nat. Energy* **2017,** *2*, 17119.

42. Wang, Y.; Yu, X.; Xu, S.; Bai, J.; Xiao, R.; Hu, Y. S.; Li, H.; Yang, X. Q.; Chen, L.; Huang, X., A zero-strain layered metal oxide as the negative electrode for long-life sodium-ion batteries. *Nat. Commun.,* **2013,** *4*, 2365.

43. Roger, M.; Morris, D. J. P.; Tennant, D. A.; Gutmann, M. J.; Goff, J. P.; Hoffmann, J. U.; Feyerherm, R.; Dudzik, E.; Prabhakaran, D.; Boothroyd, A. T.; Shannon, N.; Lake, B.; Deen, P. P., Patterning of sodium ions and the control of electrons in sodium cobaltate. *Nature* **2007,** *445*, 631.

44. Meng, Y. S.; Hinuma, Y.; Ceder, G., An investigation of the sodium patterning in Na_xCoO_2 ($0.5 \leqslant x \leqslant 1$) by density functional theory methods. *The J. Chem. Phys.* **2008,** *128* (10), 104708.

45. Kang, S. M.; Park, J.-H.; Jin, A.; Jung, Y. H.; Mun, J.; Sung, Y.-E., Na+/Vacancy Disordered P2-$Na_{0.67}Co_{1-x}Ti_xO_2$: High-Energy and High-Power Cathode Materials for Sodium Ion Batteries. *ACS Appl. Mater. Inter.,* **2018,** *10* (4), 3562-3570.

46. Zhao, C.; Lu, Y.; Chen, L.; Hu, Y.-S., Ni-based cathode materials for Na-ion batteries. *Nano Res.,* **2019,** *12* (9), 2018-2030.

47. Yabuuchi, N.; Takeuchi, M.; Nakayama, M.; Shiiba, H.; Ogawa, M.; Nakayama, K.; Ohta, T.; Endo, D.; Ozaki, T.; Inamasu, T.; Sato, K.; Komaba, S., High-capacity electrode materials for rechargeable lithium batteries: Li_3NbO_4-based system with cation-disordered rocksalt structure. *Proc. Natl. Acad. Sci.* **2015,** *112* (25), 7650.

48. Weng, B.; Xu, F.; Wang, C.; Meng, W.; Grice, C. R.; Yan, Y., A layered $Na_{1-x}Ni_yFe_{1-y}O_2$ double oxide oxygen evolution reaction electrocatalyst for highly efficient water-splitting. *Energy Environ. Sci.,* **2017,** *10* (1), 121-128.

Table of Contents

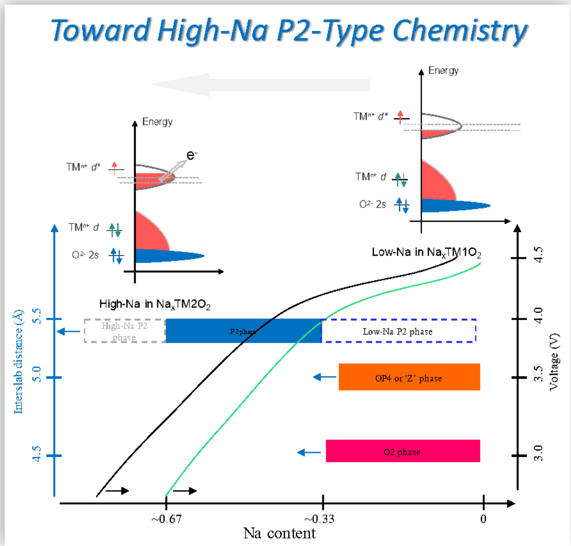

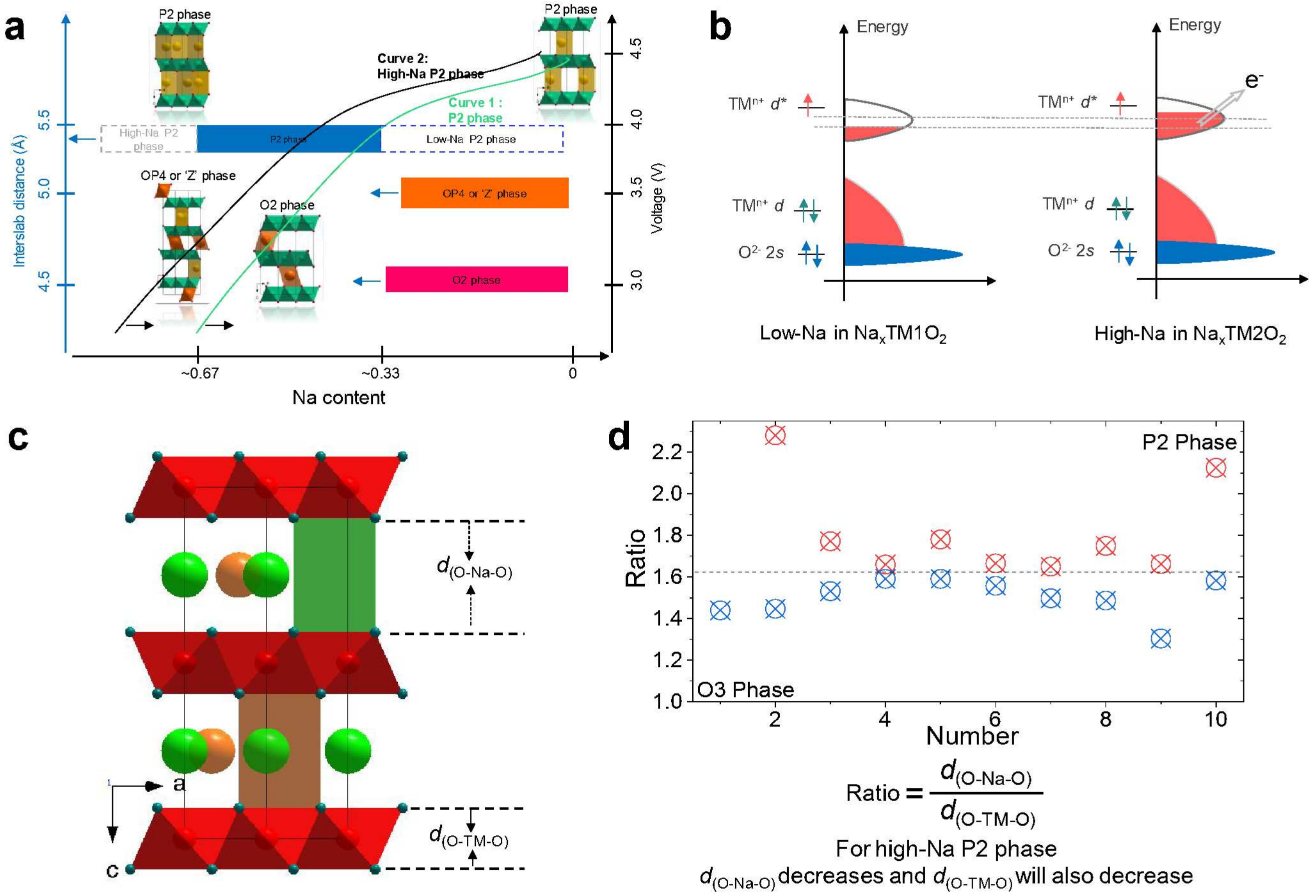

Figure 1. Possible advantages of the high-Na P2-type Na-ion cathodes and the corresponding design strategy. a. Structural evolution mechanism of high-Na P2 oxides during desodiation. **b.** The electronic structure of the low-Na and high-Na P2 oxides. **c.** Crystal structure of P2-type oxides. The interlayer distance $d_{(O\text{-}Na\text{-}O)}$ is the average perpendicular distance between the two oxygen sheets enclosing Na ions, and the interlayer distance $d_{(O\text{-}TM\text{-}O)}$ is the perpendicular distance of two parallel sheets containing transition metal (TM). **d.** The ratio between the interlayer distances of $d_{(O\text{-}Na\text{-}O)}$ and $d_{(O\text{-}TM\text{-}O)}$ for the typical P2- and O3- type compounds.

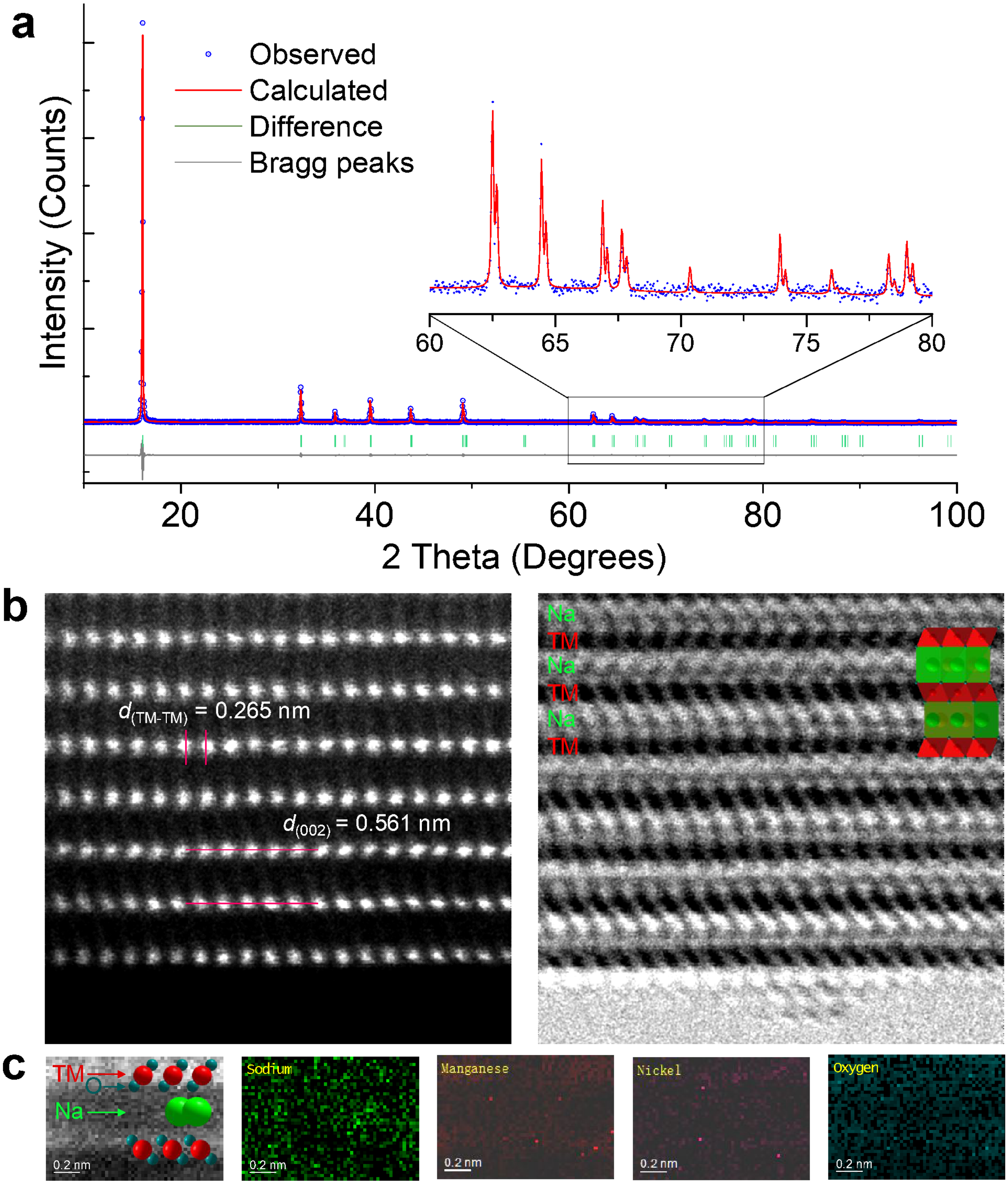

Figure 2. Structural characterization of the high Na-content P2 type oxide. a, Rietveld refinement of X-ray diffraction (XRD) pattern of $Na_{45/54}Li_{4/54}Ni_{16/54}Mn_{34/54}O_2$ (a = 2.89058(7) Å, c = 11.07541(18) Å), and the inset showing the enlarged pattern of (002) peak. **b**, Atomic-resolution high-angle annular dark field (HAADF) and annular bright field (ABF)-scanning transmission electron microscopy (STEM) images at the [010] zone axis. **c**, Electron energy loss spectroscopy (EELS) mappings of Na, Mn, Ni, and O elements.

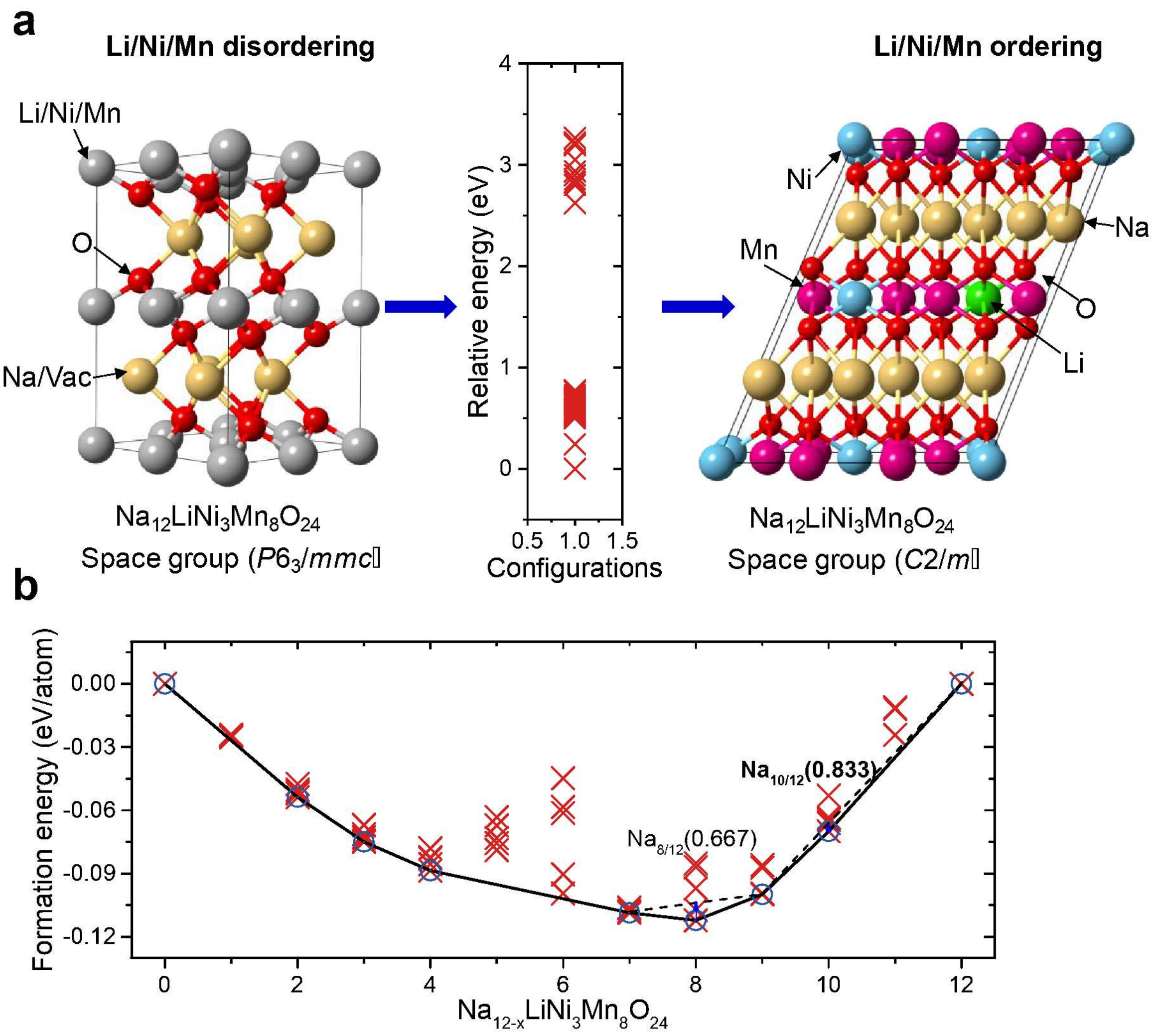

Figure 3. Determination the Na/vacancy ordering and phase stability in convex hull. **a**, Determination of the Li/Ni/Mn (dis)ordering in the system of $Na_{12-x}LiNi_3Mn_8O_{24}$. The detailed information of determination on the ground state structure and Li/Ni/Mn (dis)ordering in the system of $Na_{12-x}LiNi_3Mn_8O_{24}$ is presented in the Supporting discussion S1. **b**, Phase stability in $Na_{12-x}LiNi_3Mn_8O_{24}$-$LiNi_3Mn_8O_{24}$ convex hull. The formation energy was calculated considering all possible Na and their vacancy configurations, and the potential structures with different Na contents were predicted in this study. Red crosses indicate the energies of different enumerated phases computed at the Na content. Blue circles are ground states, as they are part of the convex energy hull in solid line.

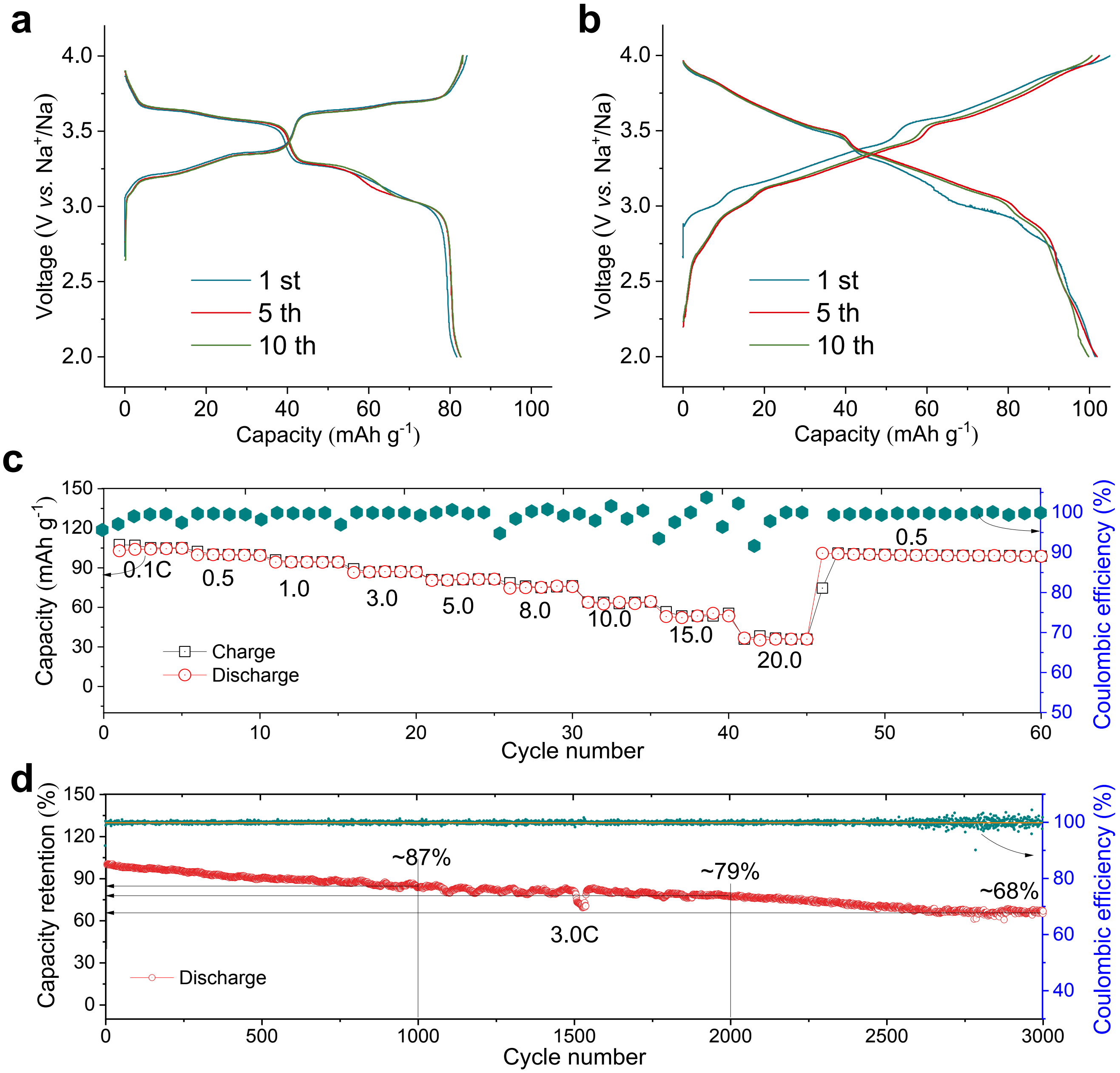

Figure 4. Electrochemical performance of high Na-content P2-type cathode. Galvanostatic charge-discharge curves of **a**, $Na_{2/3}Ni_{1/3}Mn_{2/3}O_2$ and **b**, $Na_{45/54}Li_{4/54}Ni_{16/54}Mn_{34/54}O_2$ electrodes at a rate of 0.15C (corresponding to ~22 mA g^{-1}) in the voltage range of 2.0-4.0 V *vs.* Na^+/Na. **c**, Rate capability of $Na_{45/54}Li_{4/54}Ni_{16/54}Mn_{34/54}O_2$ from 0.1C (16 mA g^{-1}) to 20C (3,200 mA g^{-1}). **c**, Discharge capacity retention of $Na_{45/54}Li_{4/54}Ni_{16/54}Mn_{34/54}O_2$ with first the three cycles at 0.1C (18 mA g^{-1}) and following cycled at 3.0C (540 mA g^{-1}). The capacity is normalized by that of 3.0C. Above 70 % capacity is retained up to 2,500 cycles with approximate 100% Coulombic efficiency (CE), but the CE is found to be unstable in the following cycles; after 3,000 cycles, ~68% capacity is remained.

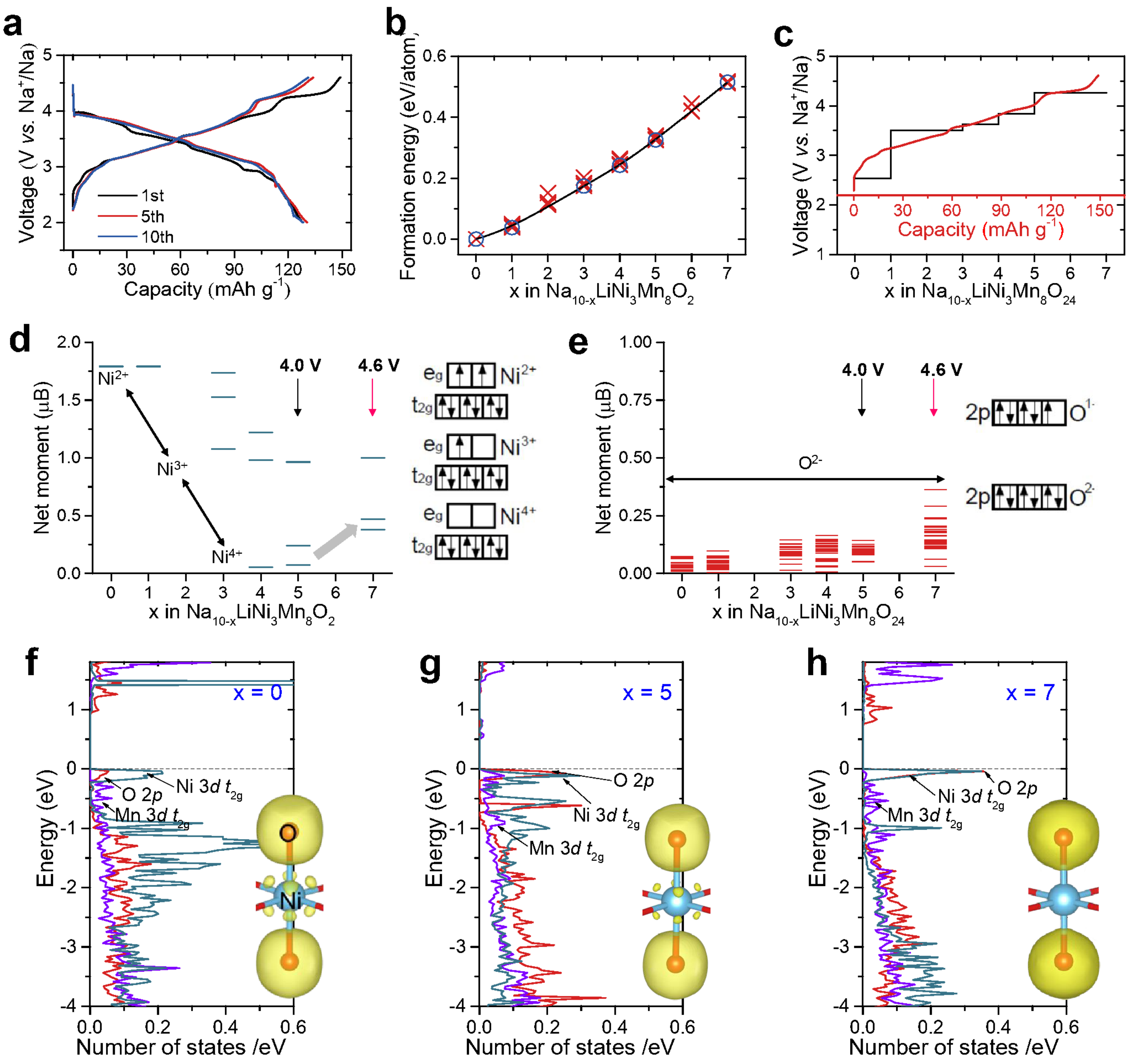

Figure 5. The desodiation process and redox sequence during the first charging process. **a**, Galvanostatic charge-discharge curves of $Na_{45/54}Ni_{16/54}Mn_{34/54}Li_{4/54}O_2$ at a rate of 0.15C in the voltage range of 2.0-4.60 V. **b** and **c**, The calculated formation energy of desodiation structures of $Na_{10-x}LiNi_3Mn_8O_{24}$ ($0 \leqslant x \leqslant 7$) convex hull and the corresponding voltage profile during the desodiation process in $Na_{45/54}Li_{4/54}Ni_{16/54}Mn_{34/54}O_2$. **d** and **e**, The magnetization and oxidation state evolution during the desodiation process of Ni and O ions in intermediate phases from $Na_{10}LiNi_3Mn_8O_{24}$ to $Na_3LiNi_3Mn_8O_{24}$. Electronic structure evolution on partial density of states (pDOS) of the Ni 3*d* t_{2g}, Mn 3*d* t_{2g} and O 2*p* orbitals of the x=0 (**f**), 5 (**g**), and 7 (**h**) in $Na_{10-x}LiNi_3Mn_8O_{24}$. The Fermi energy is set to 0 eV. Insets show the iso-surface of the charge density for the lowest unoccupied states of different desodiated states.

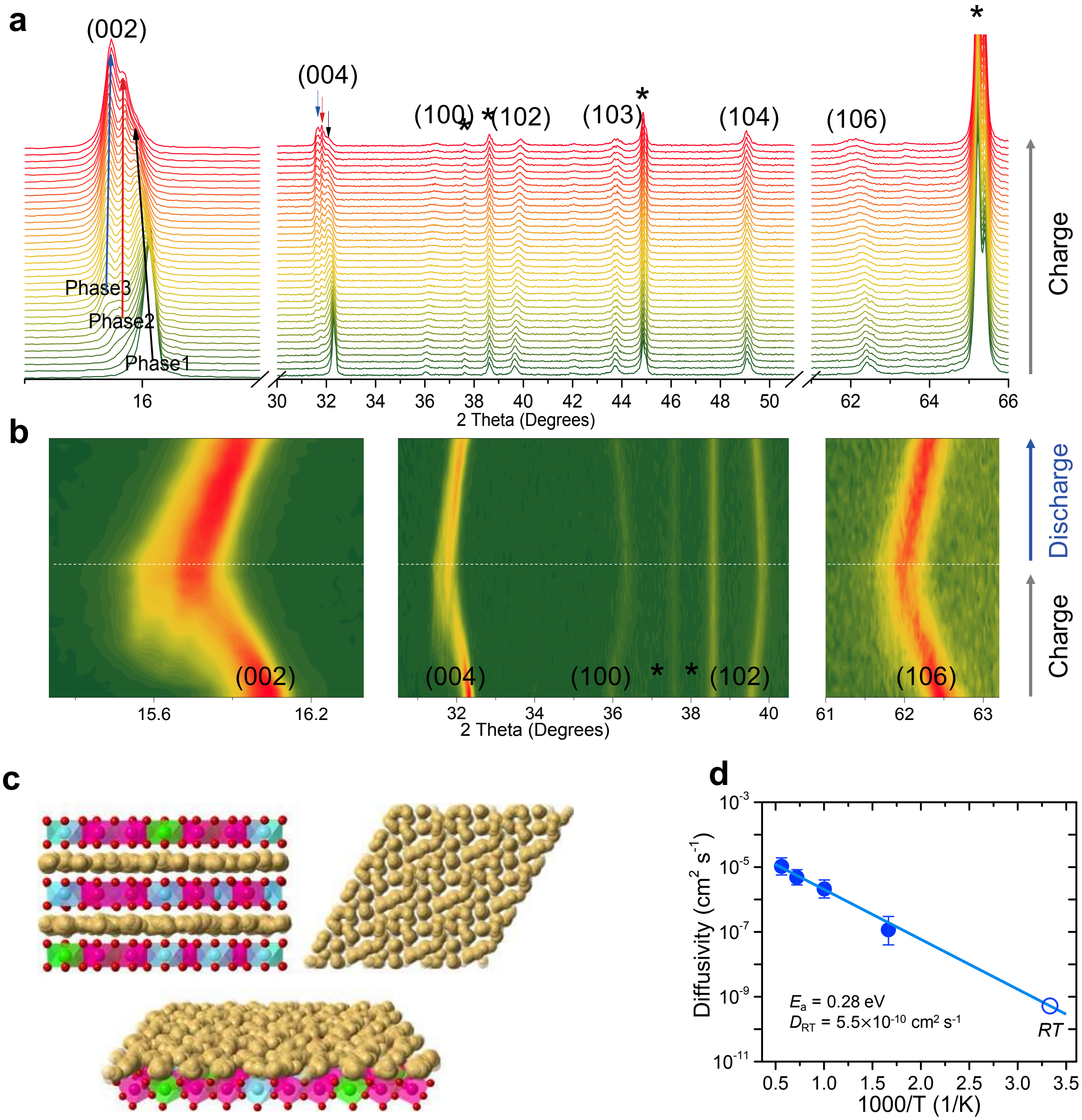

Figure 6. Structural evolution and Na⁺ ion transport properties of this P2-type cathode. a, *In-situ* XRD patterns recorded at a rate of 0.05C charged to 4.60 V. The peaks marked by an asterisk originate from the casing of the *in-situ* Swagelok cell. **b,** *In-situ* XRD patterns recorded at a high rate of 0.5C in the voltage range 2.0-4.0 V. **c**, Na⁺ migration pathway in the high Na-content P2-type oxide simulated at a temperature of ~1400 K over a period of 6 ps. The detailed views of Na⁺ layers are given in the right and below panels, where the yellow spheres indicate the trace of the Na⁺ positions during MD simulations. **d**, Arrhenius plot of diffusion coefficients resulting from the MD simulations, resulting in a Na⁺ ion migration energy barrier of 0.28 eV.

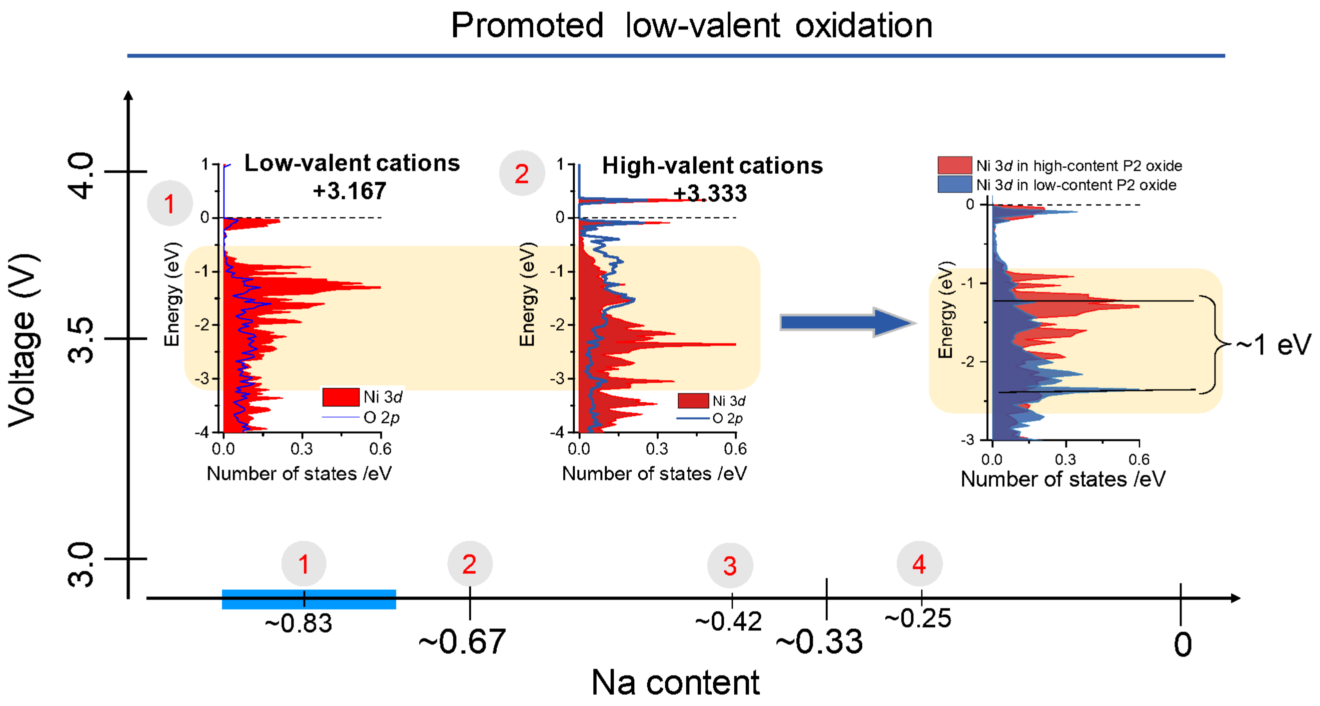

Figure 7. Illustration of the electronic evolution mechanism in the $Na_{45/54}Li_{4/54}Ni_{16/54}Mn_{34/54}O_2$ high Na-content P2-type material. The DFT predicted electronic evolution during charge (desodiation). The large amount of Na in P2-type materials reduces the average oxidation state of the TM ions below that of commonly low Na-content P2 materials. The consequence is that the low-valent cations can be oxidized to their high state more easily.